Ionics (2023) 29:1039–1052
https://doi.org/10.1007/s11581-022-04852-5

ORIGINAL PAPER

Numerical validation of direct ethanol fuel cell operating at high temperature

A. R. Q. Panesi[1] · R. P. Silva[1] · E. I. Santiago[1]

Received: 28 September 2022 / Revised: 28 November 2022 / Accepted: 2 December 2022 / Published online: 26 December 2022

Abstract

In the present work, a three-dimensional steady-state model was developed to analyze the performance of high-temperature direct ethanol fuel cell (HT-DEFC) based on polybenzimidazole (PBI) electrolytes. A non-isothermal model of a HT-DEFC setup using a PBI/H_3PO_4 membrane was employed using computational fluid dynamics (CFD). This work is aiming at a validation of experimental data of HT-DEFC prototypes based on the simulation of polarization curves. The model predicts the mole concentration of H_3PO_4, heat and current density distributions, as well as mass fraction ethanol during operation at 180 °C. The heat transfer model was coupled to the electrochemical and mass transport, allowing that a particular heating configuration was investigated considering the temperature distribution on the PBI membrane. We have found that temperature and relative humidity (RH) are mostly related to PBI properties resulting from H_3PO_4 lixiviation and conductivity decreasing as well as ethanol crossover strongly interferes on the oxygen reduction reaction (ORR) rate, leading to poor HT-DEFC performance.

Keywords HT-DEFC · PBI · CFD · Phosphoric acid · Ethanol

Introduction

Ethanol can be considered an attractive alcohol suitable as a hydrogen source for PEMFC due to substantially higher energy density of 8.00 $kWhkg^{-1}$, no toxicity, and renewability, which can mitigate degradative environmental pollution issues. Among the several fuel cell types, the proton exchange membrane fuel cells, also known as PEM fuel cells or PEMFC, are expected to play a significant role in the next-generation energy systems [1].

In general, hydrogen is the current fuel employed in PEMFCs; however, difficulties associated with H_2 storage and distribution have demanded alternative fuels. In this context, liquid fuels, such as methanol and ethanol, have been taken into account to overcome such H_2 limitations [2].

Ethanol stands out over methanol because it is considered a renewable fuel and, thus, environment friendly, with low toxicity and an easily adaptable production and distribution infrastructure, mainly for mobile applications. In this respect, the PEMFC technology also allows, obviously with some limitations, to receive ethanol as a fuel [3].

The poor DEFC performance, mainly at low temperature (< 100 °C), can be considered the main constraint of the technology. This feature is consistent with the slow ethanol oxidation kinetic, related to the difficulty in breaking C–C bonds, leading to preferential formation of CO-like intermediates with high poisoning capacity on Pt surfaces. In addition, the mixed potential caused by the ethanol crossover is also a source of a remarkable overpotential loss, mainly when state-of-the-art Nafion is used as polymeric electrolyte [4].

By considering that most of the electrode reactions are thermally activated processes, the increase of the temperature is presented as an alternative to overcome the kinetic effects observed at low temperature, contributing to the acceleration of the electrode reactions as well as lower formation of intermediates and poisoning effects. On the other hand, the strong dependence of the proton conduction in function of the water is the main limiting of the operating temperature (100 °C) for Nafion-based PEMFCs. Such a feature is resulting from a decrease of the membrane conductivity with the temperature increase, as a result of diminishing

✉ A. R. Q. Panesi
ricardopanesi@yahoo.com.br

[1] Nuclear and Energy Research Institute (IPEN-CNEN), Center of Fuel Cells and Hydrogen (CCCH), São Paulo, SP, Brazil

of water vapor pressure, and consequently of the reduction of proton charge carriers.

Polybenzimidazole (PBI) membranes have been presented as a viable alternative to replace conventional Nafion-like membranes in HT-PEMFC (high-temperature PEMFC). This feature is due to the fact that proton conduction mechanism in PBI is non-water dependent as observed for Nafion-like membranes, becoming possible to operate these devices at temperatures above 100 °C without significant loss of conductivity. PBI or poly[2,2-(m-phenylene)-5,5-bibenzimidazole is an engineering polymer known to have high mechanical, thermal, and chemical resistance result of the interactions of the benzene and imidazole rings present in the PBI monomer structure (Fig. 1).

Despite its recognized mechanical properties, PBI does not present, in the form found, the ability to transport ions, an exclusive characteristic of ionomeric polymers. In this context, the application of PBI as a solid electrolyte for HT-PEMFC is only possible by doping with inorganic acids, such as phosphoric acid (H_3PO_4) and sulfuric acid (H_2SO_4), which show some degree of ionic dissociation at high temperatures. PBI in conjunction with H_3PO_4 is a promising electrolyte for use in HT-PEMFC, as it combines excellent thermal stability of the polymer and low vapor pressure of the acid allowing use at elevated temperatures [6].

HT-PEMFC devices based on H_3PO_4-doped PBI membranes do not require complex humidification control systems [7, 8]. Numerical analysis by using CFD of tubular cathodes for LT-DEFC in terms of O_2 concentration, temperature (30–70 °C), porosity, and pressure was carried out. Summarily, the authors found that both temperature and tubular cathode configuration influence the mass transport processes, while the gas pressure reveals to slightly affect the DEFC performance [9].

Such features become PBI a promising candidate as a polymeric electrolyte for HT-DEFC (high-temperature direct ethanol fuel cell). However, some issues related to the effect of some phenomena occurring in electrodes and membranes on the performance of HT-PEMFC are open. In this context, numerical approaches can be very useful in the elucidation of drawbacks related to HT-DEFC technology, which is not clear empirically.

There are a few papers reporting CFD as a tool in the understanding of DEFC systems. It is worth noting that most of the scarce literature on DEFC is reported on low-temperature (LT) DEFC, which represents a different approach from what is presented in this work. As an example, more recently, an analysis of channel design has been also considered in CFD studies. An important finding of this work is that the optimization of porous channels, such as square vs parallel, can lead to an improvement in DEFC performance [10].

Modeling involving energy transport in fuel cells can be performed in two different ways: isothermally or non-isothermally. Non-isothermal modeling can reveal important aspects of each project in relation to the temperature distribution in the cell. Uniform temperatures are generally related to better performance in DMFCs, which can also be true for DEFCs. In addition, water management can contribute positively or negatively to proton conduction phenomena, which is important to have a photograph of the water movement in HT-DEFC. Other parameters, such as temperature and current distribution, can also contribute to the elucidation of the phenomena involved in HT-DEFC [11].

In addition, a comprehensive study involving CFD analysis in DEFC was conducted by Sokmez et al. The main conclusion of this work is that the operation conditions affect more significantly the DEFC performance than design parameters [12].

In this paper, a three-dimensional, non-isothermal model is presented to describe the processes occurring in components of H_3PO_4-doped PBI-based HT-DEFC. To the best of our knowledge, it is the first time that a work of validation of experimental data of HT-DEFC taking into account a very robust three-dimensional model has been carried out.

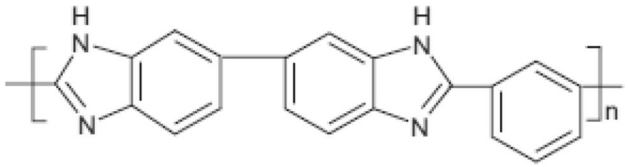

Fig. 1 PBI monomer structure. Adapted from [5]

Methodology

Experimental analysis

The PBI membranes were prepared by the method known as casting using commercial PBI (Celazole®) solid, in solvent N, N′-dimethyl-ketamide (DMAc) using 40 mg of lithium chloride for each dissolution of PBI (0.75 g of PBI by dissolving in DMAc. To eliminate the solvent, the system was subjected to heat treatment for 120 °C for 6 h. Subsequently, the membrane was washed in boiled water to remove any trace of the solvent and stabilizer [13]. The next step to the formation of the membranes is doping with phosphoric acid to increase the proton conductivity, in which the doping agent in the PBI membranes is H_3PO_4. The doping process was carried out by immersing the PBI membrane in a 10 $molL^{-1}$ phosphoric acid solution. The membrane-electrode assembly (MEA) was prepared with 4 × 4 cm membrane and gas diffusion electrodes (GDE) with 5 cm^2 catalyst area

with 1 mg Ptcm^{-2} of Pt/C 40% catalyst. Anode and cathode electrodes were with same catalyst loading. The fuel cell was assembled with serpentine gas flow pattern as shown in Fig. 5. Different parameters as level of membrane doping and loading of catalyst were tested using hydrogen (anode) and oxygen (cathode) and results discussed elsewhere [11].

The fuel cell tests were divided into 2 experiments for the same MEA: (1) previous activation with pure H_2 and O_2 and (2) DEFC tests itself. The catalytic sites are activated by raising polarization curves with pure H_2 and O_2 at 180 °C. Prior to ethanol tests, the single cell was heated at 180 °C and, after stabilization, fed with hydrogen and oxygen as activation protocol. In this process, the current was applied ranging from 0.01 to 0.1 A, with a current step of 0.01 A, 0.2 to 2.0 A with 0.1 A step, and 2.2 to 10 A using 0.2 A step. Considering that HT-PEMFC has higher performance—and consequently a higher limiting current—than that provided by DEFC, a final current of 10A is easily reached. On the other hand, the performance is appreciably low for DEFC, which leads to a low limiting current. The DEFC was directly fed with 5.7 molL^{-1} ethanol solution, and flux was in vapor form (vaporizer at 180 °C) of 2 mLmin^{-1}. Three polarization curves were obtained in sequence to evaluate both the performance and reproducibility of the HT-DEFCs. Values of the electric potential difference (ΔE) were collected (galvanostatic mode) by means of dynamic charge and a multimeter connected to the current collector plates. After stabilization of the cell temperature and the open circuit voltage (OCV), the current was applied ranging from 0.01 to 0.1 A, with a current step of 0.01 A, 0.2 to 2.0 A with 0.1 A step. All potential values were collected after 10 s of applied current. OCV was collected after 5 min of stabilization (Fig. 2).

Model development

Using computational fluid dynamics (CFD) software, models can be evaluated in numerical investigation involved in fuel cell tests. Moreover, mathematical models can be perceived as critical tools, which can be beneficial for the comprehension and investigation of the areas which pose as challenges to the HT-PEMFCs technology.

For this analysis, modeling and simulation were performed in COMSOL Multiphysics 5.3a software, which was used to build a single-phase non-isothermal and tridimensional fuel cell model with finite element method. For this model, the following conditions were assumed: steady state, ideal gas mixtures, fluid compressible, and laminar flow, and electro-osmotic drag was considered negligible. The calculation domain consisted of gas channels, gas diffusion layers (GDLs), catalytic layers (CLs), membrane (mem), and bipolar plates (BPs), as seen in Fig. 3.

Figure 4 depicts the magnified model geometry (Fig. 4a), and a representation of mesh determination hierarchy (Fig. 4b) flowchart is shown, and the naming convention for the domains and the boundaries is presented. The flowchart depicted in Fig. 4B represents the hierarchy used for the mesh determination. The mesh of this simulation uses tetrahedral with over 864,559 elements to fill the model.

The mesh configuration was customized and followed the hierarchy established as described in Fig. 4B:

1- Definition of "normal" size, with fluid dynamic calibration in all domains
2- Size setting to "fine," with fluid dynamic calibration for domains 1, 2, 6, and 7

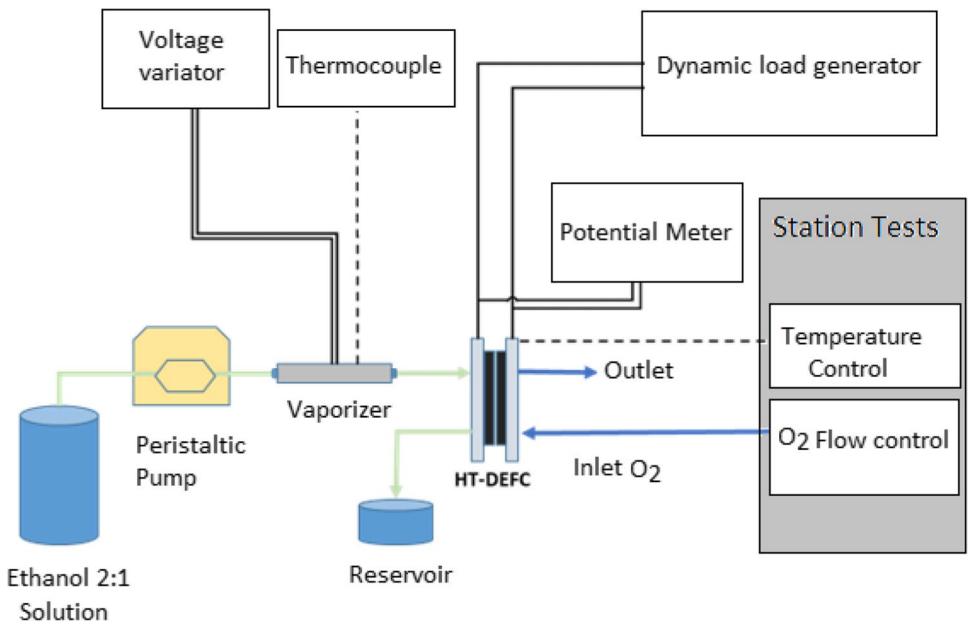

Fig. 2 Experimental apparatus

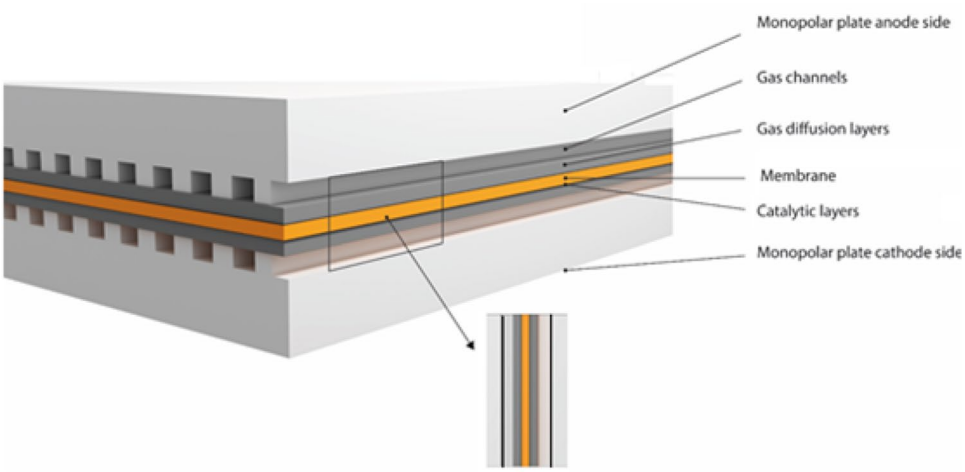

Fig. 3 Generic schematic model of a PEM fuel cell

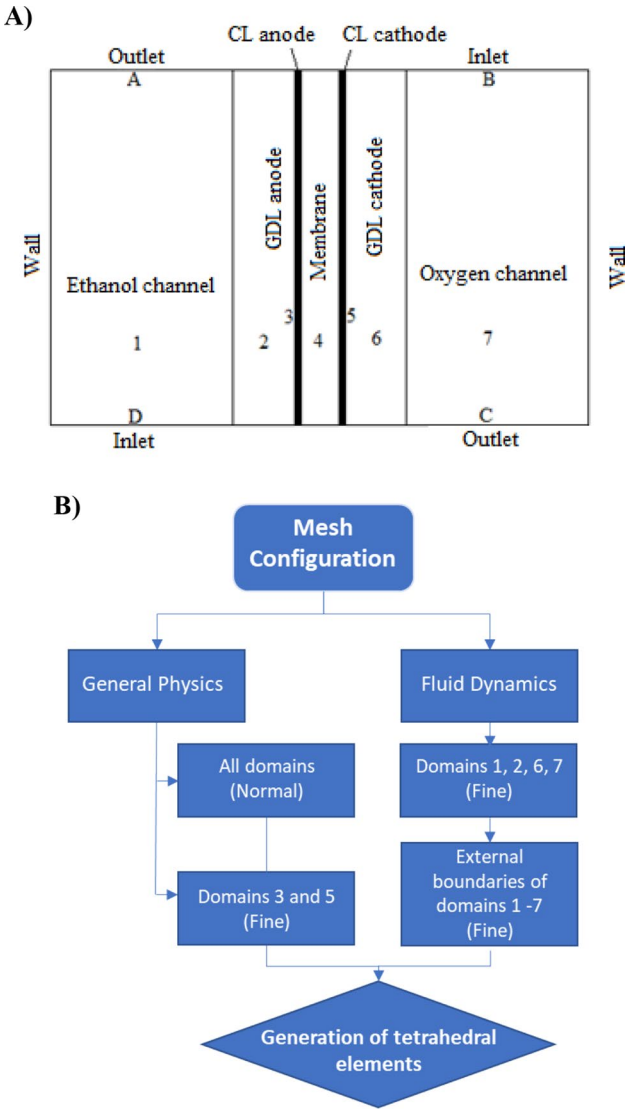

Fig. 4 **A** Model geometry and naming convention and **B** mesh determination flowchart

3- Size setting to "fine," with general physics calibration for domains 3 and 5
4- Size setting to "fine," with fluid dynamic calibration for the external boundaries of domains 1 to 7 and the contact boundaries of the monopolar plates
5- Generation of tetrahedral elements in all domains

A parametric solver was used for the construction of the polarization curves. The model was solved considering steady state, ideal gas mixtures, fluid compressible, and laminar flow as well as electro-osmotic drag was considered negligible. The segregated method with 8 steps specified below was used:

- Steps 1 and 2 are responsible for the moment transport variables solving the velocity and pressure fields: they consist of GMRES (generalized minimal residual method) geometric multigrid linear solvers with a residual tolerance of 0.001 and a maximum number of 150 iterations.
- Step 3 is responsible for the transport of charges and consists of a direct solver of linear equations of the MUMPS type (MUltifrontal Massively Parallel Sparse) with a memory allocation factor of 1.2.
- Steps 4 and 5 are responsible for the transport of species (O_2, H_2O, and C_2H_5OH) solving their respective mass fractions: they consist of GMRES-type interactive linear solvers, with a residual tolerance of 0.001 and a maximum number of 150 iterations.
- Step 6 is responsible for the heat transport by solving the temperature field that consists of GMRES-type geometric multigrid linear solvers with a residual tolerance of 0.001 and a maximum number of 150 iterations.
- Steps 7 and 8 are responsible for the transport of species (H_2PO_4) solving their respective mass fractions: they consist of GMRES-type iterative linear solvers,

Table 1 Parameter, boundary, and initial values regarding the conservation of mass and momentum

Domain	Initial value
1, 2, 3	$\vec{V} = 0, P = 101.325Pa$
5, 6, 7	$\vec{V} = 0, P = 101.325Pa$
Boundary	Condition
A	$P = 0$
B	Q_{O_2}
C	$P = 0$
D	$Q_{C_2H_5OH}$
Wall	Condition
Anode	$\vec{V} = 0$, no slip
Cathode	$\vec{V} = 0$, no slip
Source	*Term
2, 3, 5, 6	$-\frac{\mu}{k}\vec{V}\epsilon$
3	$-M_{C_2H_5OH}\frac{J_a}{12F}$
5	$M_{H_2O}\frac{J_c}{2F} - M_{O_2}\frac{J_c}{4F}$

*μ = dynamic viscosity, k = permeability, ϵ = porosity

Table 2 Parameter, boundary, and initial values regarding the conservation of species

Domain	Initial value
1, 2, 3	$w_{C_2H_5OHin}$
5, 6, 7	$wO_{2\text{in}}$
Boundary	Condition
A	$J_i = 0$
B	$wO_{2\text{in}}$
C	$J_i = 0$
D	$w_{C_2H_5OHin}$
Source	Term
3	$-M_{C_2H_5OH}\frac{J_a}{12F}$
5	$M_{H_2O}\frac{J_c}{2F} - M_{O_2}\frac{J_c}{4F}$

Table 3 Parameter, boundary, and initial values regarding the conservation of charges

Domain	Initial value
2, 3, 5, 6	$E = 0V$
Wall	Condition
Anode	$E = 0V$
Cathode	$E = Ecel$
Source	Term
3	$-i_a$
5	i_c

with a residual tolerance of 0.001 and a maximum number of 150 iterations.

Tables 1, 2, 3, and 4 present the parameters for calculating the conservation of mass, momentum, species, charge, and energy.

The dimensions of the cell components with 5-cm^2 active area serpentine flow field are listed in Table 5. Furthermore, the parameters considered in the development of models are represented in Table 6.

The complete drawing of 2-D four serpentine channels geometry type for HT-PEMFC modeling is shown in Fig. 5.

Table 4 Parameter, boundary, and initial values regarding the conservation of energy

Domain	Initial value
1, 2, 3, 4, 5, 6, 7	$T = T0$
Boundary	Condition
A	$-nq = 0$
B	$T = 293.15K, P = 101.325Pa$
C	$-nq = 0$
D	$T = 293.15K, P = 101.325Pa$
Source	Term
3	$i_{0a}\left(\eta_a + T\frac{dE_{eq}}{dT}\right) + \frac{{i_a}^2}{k}$
4	$\frac{i^2}{k}$
5	$i_{0c}\left(\eta_c + T\frac{dE_{eq}}{dT}\right) + \frac{{i_c}^2}{k}$

Table 5 Geometrical parameters of the model

Parameter	Value (mm)
Flow channel length	22.55
Flow channel width	0.8
Flow channel height	1.0
Rib width	0.65
Monopolar plate thickness	11
GDL thickness	0.454 [14]
Catalyst layer thickness	0.012
Membrane thickness	0.060

General equations

Mass and momentum conservation

Considering the fuel cell as a volume control, there is mass transferred through the system in the form of ethanol, oxygen, and water. Reagent flow in the fuel cell flow channels depends on the design of the channels, such as, for example, shape and dimensions. In the electrode and membrane layers, reagents can be transferred by convection and diffusion. Regardless of the mode of transport, the governing equations are still the same [38]. The general equation for conservation of mass, which is within a fuel cell, such as fluid flow, diffusion, and phase change, is:

$$\frac{\partial \rho}{\partial t} + \nabla\left(\rho\vec{V}\right) = 0 \quad (1)$$

Table 6 Physiochemical and transport properties

Parameter	Value
Membrane conductivity	1 Sm^{-1}*
Electronic conductivity in the GDL, BP	66,700, 3000 Sm^{-1}[15–17]
Permeability of GDL, CL	1.18×10^{-11} m^2, 10^{-13} m^2 [18]
Volume fraction of electrolyte in CL	0.55 [19]
Thermal conductivities of GDL, CL, membrane, BP	1.2, 1.5, 0.95, 20 W m^{-1} K^{-1} [20–22]
Reference exchange current density at anode	1×10^{5} Am^{-2} [23–25]
Reference exchange current density at cathode	1.8×10^{-4} Am^{-2} [26, 27]
Cathodic Tafel slope	100 $mVdec^{-1}$ [28, 29]
Anode transfer coefficient	0.5 [30]
Cathode transfer coefficient	1.0 [31, 32]
Pt loading	0.01 kgm^{-2}
Acid doping level	120%
Ethanol feed concentration	5.6 $molL^{-1}$
Density of GDL, CL, membrane, BP	1743.8, 1000, 1300, 1580 kg m^{-3} [23–25]
Operating pressure and temperature	101.325 kPa, 453.15 K
Porosity of GDL, CL	0.8, 0.25 [14, 33]
Specific heat capacities of GDL, CL, membrane, BP	568, 3300, 1650, 1580 J kg^{-1} K^{-1} [6–8]
Diffusion of O_2 in H_3PO_4	1.65×10^{-9} m^2 s^{-1}[20, 34–36]
Diffusion coefficient of ethanol in water	5×10^{-10} m^2s^{-1} [37]
O_2 -H_2O Binary diffusion coefficient	3.80×10^{-5} m^2 s^{-1}[27]

*The conductivity used in the numerical simulation was determined experimentally by using four-probe impedance spectroscopy at different temperatures (100 to 200 °C). The tests were performed on a frequency analyzer in the frequency range from 100 Hz to 1 MHz and amplitude of 200 mV. For humidity control, the homemade sample holder was initially dried at a temperature of 150 °C for 1 h prior to the tests. After cooling, the sample was inserted into the system and heated to 100 °C. Readings were taken every 10 °C, waiting 10 min for stabilization for measurement up to 200 °C

The first term represents accumulation of mass with time, and the second term describes the net flow of mass out of the element across its boundaries and is called the convective term. The conservation of momentum is required to model the fluid velocity and species partial pressures. Momentum conservation for fluid compressible is described by flow channels:

$$\frac{\partial\left(\rho\vec{V}\right)}{\partial t}+\nabla\left(\rho\vec{V}\vec{V}\right)=-\nabla p+\nabla\left[\mu\left(\nabla\vec{V}+\left(\nabla\vec{V}\right)^{T}-\frac{2}{3}\left(\nabla.\vec{V}\right)\mathrm{I}\right)\right]+S_m \quad (2)$$

The left side in Eq. (2), the first term describes the accumulation of momentum as a function of time, and the second term is associated with the advective term flux. On the right side, the first term represents the pressure gradient and the second term viscous stress tensor. The source term, S_m, is different for different regions of the fuel cell as shown in Table 1. The ρ and $\vec{V}$ terms denote the mixture density and superficial fluid velocity respectively as well as μ is the dynamic viscosity, ε is the porosity, and k is the permeability of the porous medium.

The Brinkman Eq. (3) describes the gas flow within porous medium, i.e., GDL and CL. This mathematical model extends Darcy's law to include a term that accounts for the viscous transport in the momentum balance, and it treats both the pressure and the flow-velocity vector as independent variables:

$$\begin{aligned}\frac{\rho}{\epsilon}\left(\frac{\partial\vec{V}}{\partial t}+\left(\vec{V}\nabla\right)\right)\frac{\vec{V}}{\epsilon}=&\\ -\nabla p+\nabla\left[\frac{\mu}{\epsilon}\left(\nabla\vec{V}+\left(\nabla\vec{V}\right)^{T}-\frac{2}{3}\left(\nabla.\vec{V}\right)\mathrm{I}\right)\right]&\\ -\left(\frac{\mu}{k}+\beta\left|\vec{V}\right|+\frac{S_\phi}{\epsilon^2}\right)\vec{V}+F&\end{aligned} \quad (3)$$

Species conservation

The species considered in the model were H_2O and C_2H_5OH (ethanol) in the anode compartment and O_2, H_2O in the cathode compartment, together with the definition of the total mass flux N_i for each species i of the mixture:

$$\frac{\partial}{\partial t}\left(\epsilon\rho\omega_i\right)+\nabla\left(\epsilon\rho\omega_i\vec{V}\right)=-\nabla.J_i+S_s \quad (4)$$

$$N_i=J_i+\rho\vec{V}\omega_i \quad (5)$$

In Eq. (4), the first two terms in the species conservation equation represent species accumulation and advection

terms, and the first term on the right-hand side represents Fickian diffusion of species in porous medium. In the same way, ω_i is the mass fraction of species, and J_i is the diffusion flux. The source term S_s is equal to zero everywhere except in the catalyst layers where the species are consumed or generated in the electrochemical reactions (see Table 2).

In Eq. (5), N_i is the total mass flux vector for each species i. The diffusion model adopted on the anode side as on the cathode was the Fick's law model with the following equations:

$$J_i = -\left(\rho D_i^{fk} \nabla \omega_i + \rho \omega_i D_i^{fk} \frac{\nabla M}{M} + D_i^T \frac{\nabla T}{T}\right) \tag{6}$$

where D_i^T is the thermal diffusion coefficient and the effective diffusivity D_i^{fk} is obtained by:

$$D_i^{fk} = \left(\frac{1}{D_i^f} + \frac{1}{D_i^k}\right)^{-1} \tag{7}$$

In addition, D_i^{fk}, which represents a general diffusion matrix (SI unit: $m^2 s^{-1}$), can be described the diffusion of species i into the mixture and the Knudsen diffusion coefficient, respectively:

$$D_i^f = \frac{1 - \omega_i}{\sum_{k \neq i} \chi_{k/D_{ejk}}} \tag{8}$$

$$D_i^k = \frac{\lambda_i}{3} \sqrt{\frac{8RT}{\pi M_i}} \tag{9}$$

where D_{ejk} are the binary diffusion coefficients and λ is the mean free path average distance a particle travels between collisions. The diffusivity of oxygen in PBI is related to oxygen diffusivity in phosphoric acid and acid doping level. Thus, it can be given as [21, 34–36]:

$$D_{O_2}^{PBI} = \left(\epsilon_{PBI}\right)^{1.8} D_{O_2}^{H_{3PO_4}} \tag{10}$$

where ϵ_{PBI} is the volume fraction of electrolyte in CL. The transport properties of oxygen in concentrated phosphoric acid are related to the temperature and the acid concentration mass fraction ($m_{H_{3PO_4}}$):

$$D_{O_2}^{H_{3PO_4}} = 10^{-9} exp\left[\frac{-192.55\left(m_{H_{3PO_4}}\right)^2 + 323.55\left(m_{H_{3PO_4}}\right) - 125.61 + 62010\left(m_{H_{3PO_4}}\right)^2 - 105503\left(m_{H_{3PO_4}}\right) + 40929}{T}\right] \tag{11}$$

Already, the ethanol diffusivity was considered in water (see Table 2). The rates (mol.s) at the anode and cathode are given by:

$$\dot{n}_{H_2Oa} = \frac{j}{F} \tag{12}$$

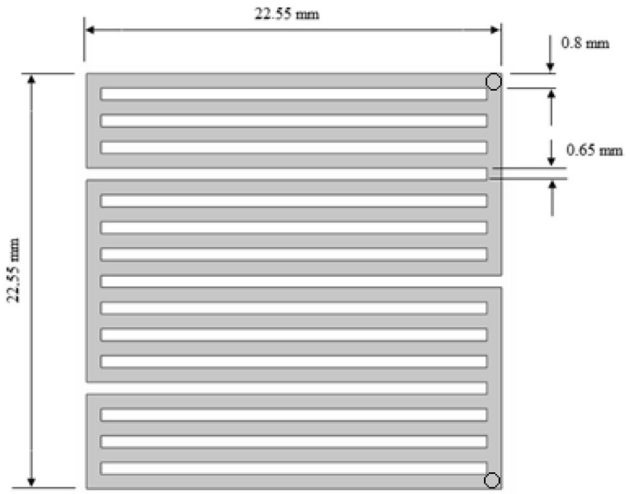

Fig. 5 2-D drawing of four serpentine flow channel geometry

$$\dot{n}_{O_2} = \frac{j}{4F} \tag{13}$$

$$\dot{n}_{C_2H_5OH} = \frac{j}{12F} \tag{14}$$

$$\dot{n}_{H_2Oc} = \frac{j}{2F} \tag{15}$$

Charge conservation

In the operation of fuel cells, charge transport is governed by Ohm's Law, where in electrochemical cells, two different types of electrical charges are present: ionic or protons (H^+), in the case of PEMFCs, responsible for charge compensation in response to the electric field generated in the electrolyte and electrons (e^-) transferred during the oxidation–reduction processes in the electrodes. Thus, an electronic potential (ϕ_{sol}) and a proton potential (ϕ_{mem}) at different locations in the computational domain must be considered. The two potentials can be written as:

$$i + (\sigma_{sol} \nabla \phi_{sol}) - S_{sol} = 0 \tag{16}$$

$$i + (\sigma_{mem} \nabla \phi_{mem}) - S_{mem} = 0 \tag{17}$$

where the potential "sol" is responsible for the transport of electrons through the solid materials of the electrode and the "mem" represents the potential transport of protons through the membrane; σ_{sol} and σ_{mem} are the electronic conductivities of the electrodes and ionic conductivity of the membrane, respectively. The source term S_{sol} and S_{mem} represent the volumetric transfer current.

The currents generated (i) are the results of electrochemical reactions that occur in the catalytic layer next to the membrane, whose phenomenon depends on the potential difference between the solid matrix of the electrode and the membrane. In this way, the exponentials in the Butler-Volmer equation can be linearized:

$$i_a = j_{0a} \tag{18}$$

Equation (18) according to COMSOL [39] can be used in regimes close to equilibrium, corresponding to small values of ($\eta \ll RT/F$) where α_{ac} are the cathode and anodic transfer coefficients.

Using a linearized Butler-Volmer reaction can be advantageous when investigating convergence issues of a model. The anodic overpotential η_a is given by:

$$\eta_a = \phi_s - \phi_l - E_{eq} \tag{19}$$

where E_{eq} is the equilibrium potential of the reaction and the subscripts of the potentials are l for the electrolyte and s for the electrode, respectively. The equilibrium potential of the electrode is zero on the anode side, and it equals the theoretical cell potential at given temperature and pressure on the cathode. The anodic and cathodic exchange current densities are given by:

$$i_{0a} = i_{0aref} \frac{P_{H_2}}{P} \tag{20}$$

$$i_{0c} = i_{0cref} \frac{P_{O_2}}{P} \tag{21}$$

where i_{0ref} is the reference electric current density, P_{H2} and P_{O2} are the partial pressure of hydrogen and oxygen, and P is the reference pressure. The cathodic kinetics can be expressed as:

$$i_c = -i_{0c} x 10^{\eta_c / b} \tag{22}$$

where b is the Tafel coefficient.

Energy conservation

In principle, the first law of thermodynamics is simply a statement that the total energy of a system is conserved, and therefore the only way in which the amount of energy can change is if the energy crosses its boundary. One of the main goals in an analysis of heat conduction is to determine the temperature range in a medium resulting from conditions imposed on its boundaries. That is, we want to know the temperature distribution or temperature field, which represents how the temperature varies with the position in the middle on the membrane surface. Once this distribution is known, the heat flux by conduction (conductive thermal flux) at any point in the medium or on its surface can be determined using the general form of conservation of energy in terms of temperature:

$$\rho c_p \frac{\partial T}{\partial t} + \nabla \left(\rho c_p \vec{V} T \right) = \nabla \left(k \vec{\nabla} T \right) + S_e \tag{23}$$

In Eq. (23), T is operating temperature, c_p is the specific heat, and k is the effective thermal conductivity. The first term on the left side describes the change in internal energy, and the second term describes the heat transfer in the fluid velocity field. On the right side, the first term corresponds to Fourier's law diffusion equation, and the second term S_e is the source term in Wm^{-3} as shown in Table 3. At the free boundaries of the fuel cell, a convective flow condition imposed in the simulations was defined as one of the boundary condition requirements:

$$-n.q = h\left(T_{ext} - T\right) \tag{24}$$

where (T_{ext}) is the ambient reference temperature (in general 273.15 K) and (h) is the convection heat transfer coefficient, using the mean values suggested by Kreith and Bohn [40] (between 15 at $30 Wm^{-2}$ K). There are five source terms, S_m, S_s, S_e, S_{sol}, and S_{mem}, which represent various volumetric sources or sinks arising from each sub-region of a fuel cell. Details of the various source terms are summarized in Table 3.

The H_3PO_4 concentration within the MEA is expected to change during cell operation. In [41], a correlating equation for H_3PO_4 vapor pressure is given (80–101 wt % acid in the range of 130–170 °C). From their experimental data, Souza et al. [42] generated an equation that coupled concentration and water vapor partial pressure:

$$X_{H3PO4} = \frac{ln\left(P_{H2O}\right) + \frac{2765.1}{T} - 22.002}{\frac{-4121.9}{T} + 2.5929} \tag{25}$$

where P_{H2O} is the water vapor partial pressure and X_{H3PO4} is mole fraction of H_3PO_4.

Results and discussion

Figure 6 compares model predictions with the corresponding experimental data for a DEFC fuel cell operating at 180 °C. It is evidenced a good approximation between the simulated

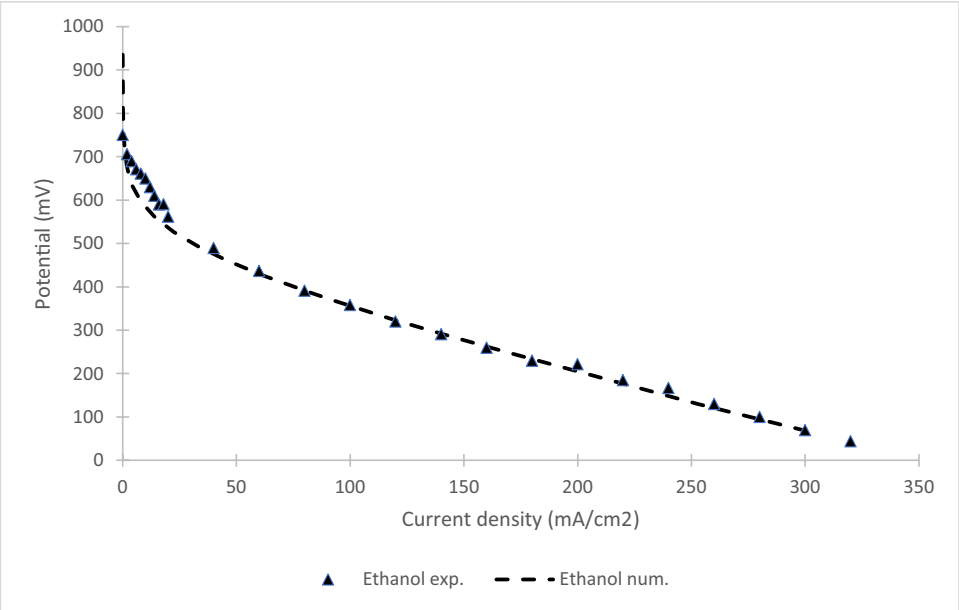

Fig. 6 Polarization curve: comparison of simulations and experiments

and experimental curves. In ethanol/oxygen, the cell was operated at constant temperature and without any humidification. The HT-DEFC performance decreases considerably when compared to that for hydrogen as a fuel as a result of the by-product formation, including acetaldehyde, acetic acid, and ethyl acetate. Such by-products are a consequence of the catalytic inefficiency to promote the rupture of the C–C bonds [3].

A slightly difference in polarization profile is evidenced in current density of up to 30 $mAcm^{-2}$. This initial region, which corresponds to activation polarization, is associated with the slowness of the reactions taking place on the surface of the electrodes. It was expected an "ideal" Butler-Volmer (exponential) profile, which experimentally was not found. Indeed, the experimental curve presents a "more linear" profile, which can be associated with unbalance in the rates involving the ethanol vapor feeding on the electrode surface (adsorption) and proton conduction by the PBI membrane, leading to variations in the potential response. Also, it is a strong indicative of the presence of mixed potential resulting from ethanol crossover.

Temperature distribution analysis

On the other hand, the temperature distribution through the membrane is a very important consideration for modulating the operation conditions and achieving better performances. Moreover, it can be useful to predict possible problems concerning thermal stresses and hot spots, especially on the membrane surface. The heating strategy considered for the start-up of the HT-PEMFC is based on one of the common methods, i.e., the heat input flux refers to the external heat that is required from the heating element (electrical resistances) to raise the maximum membrane temperature to reach 180 °C. Figure 7 shows the temperature distribution within the membrane where the anode and cathode inlet temperatures are set at 180 °C. We intend to study the most adverse possible condition of the system exactly in order to more precisely analyze the effects of the HT-DEFC operating parameters in the temperature and current distributions. In this case, the harshest condition would be the one with the highest current density, which means at cell potential of 90 mV.

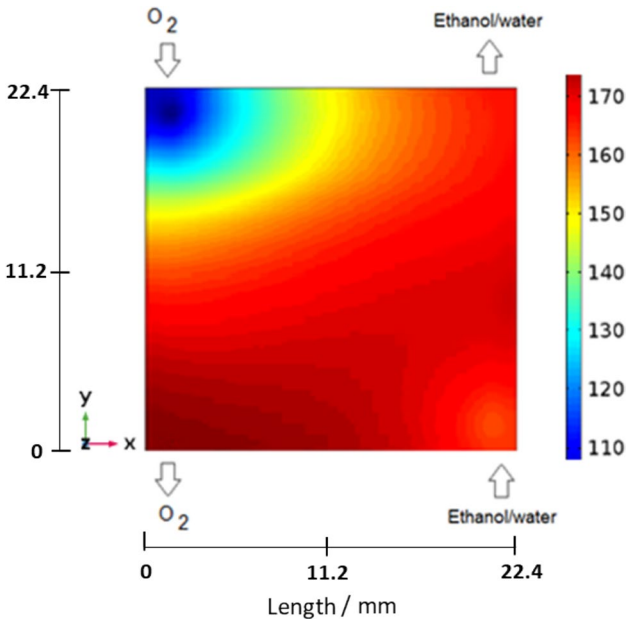

Fig. 7 Temperature distribution (°C) in the middle of the membrane at 90 mV

In addition, it can be seen appreciable difference in temperatures between the central region and regions closer to the inlet and outlet of flow channels, indicating that the temperature distribution of the membrane is also governed by inlet reactant temperature. Besides that, the region closes to the cathode inlet shows a temperature of 120 °C. In fact, the lowest temperature occurs at the regions closer to the cathode inlet rather than the anode inlet. This is probably due to the lower thermal conductivity of oxygen relative to ethanol. Also, the temperature at the cathode outlet is higher due to practically to the heat of electrochemical reactions and the evaporation of water. In addition, this is due mainly to the phenomenon of ethanol crossing through the membrane (crossover). The negative effects of ethanol crossover include decrease in the cathode potential and reduced overall efficiency [43]. Temperature analyses are very similar to results using hydrogen as fuel [11].

Current density distributions

Figure 8 shows the electrode current density magnitude for a cell operation conditions at 90, 286, and 426 mV. All of the three operating conditions have similar current density distributions with higher values that are observed near the edges of the catalyst-membrane interface, especially towards the inlet and outlet regions. The current distribution is quite similar for all the potentials studied. As expected, current density at 90 mV, which is the condition in which the processes involved, i.e., electron transfer, ionic conduction, and species diffusion occur at higher rate (maximum current density), the effects on the current distribution are more notable with current concentration achieving the maximum values (0.45 for 90 mV, 0.24 for 286 mV, and 0.1 for 426 mV). These data show that the current distribution is primarily governed by the operating conditions of HT-DEFCs. The different potentials were evaluated in all simulation results, and the same trend was evidenced.

This is reasonable because the water vapor needs to diffuse through the porous medium towards the gas flow channels before leaving the cell. Reactants flow at higher rate through peripheral channels, while smaller amounts circulate through central zones. Therefore, oxygen depletes very quickly in channels with low oxygen rates, and then water vapor concentration grows fast, causing both a lower oxygen concentration at catalyst active sites and more difficult oxygen diffusion due to water presence. This uneven distribution induces an inefficient use of electrode area probably caused by ethanol crossover. Also, the temperature variation increased with the increase of current density, where the temperature variation is greater in this model.

Phosphoric acid distribution analysis

Because of the varying humidity within a fuel cell, it is difficult to estimate the in situ concentration of H_3PO_4 acid

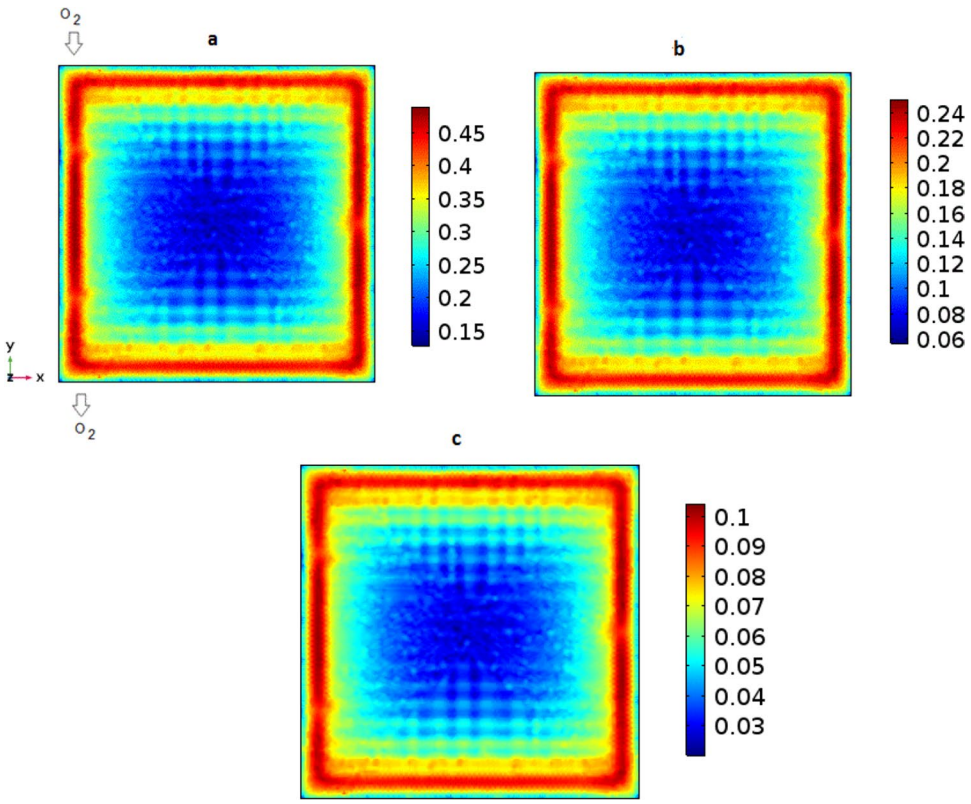

Fig. 8 Current density distribution (Acm^{-2}) at the catalyst-membrane interface on the cathode side. **a** 90 mV, **b** 280 mV, **c** 426 mV

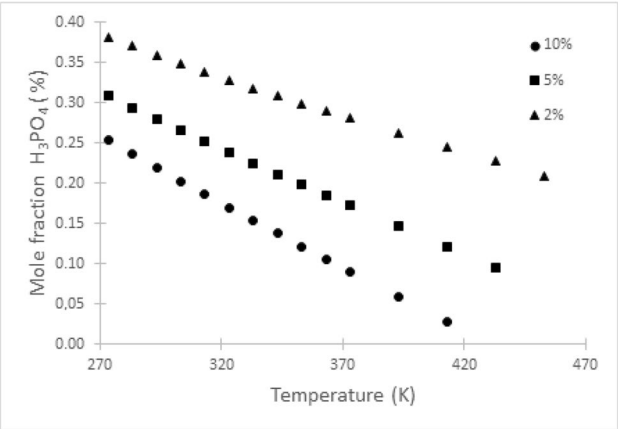

Fig. 9 Influence of the temperature and relative humidity on the mole fraction of H_3PO_4

mixture. Also, for ethanol as a fuel, the concentration of H_3PO_4 depends on the temperature and on the relative humidity. The mole fraction of H_3PO_4 was calculated using Eq. (25), and the resulting data are presented in Fig. 9. Such information is important to identify and separate possible intrinsic effects of the H_3PO_4 solution and those related to alteration at electrode-membrane resulting from fuel cell environment. Figure 9 shows that the H_3PO_4 mole fraction is strongly influenced by temperature and relative humidity (RH), in which a remarkable decrease of H_3PO_4 mole fraction with both temperature and RH is evidenced [44]. This result indicates that the concentration of phosphoric acid in the membrane can vary according to the intensities of the partial pressure of water vapor over the acidic solution, as has also been demonstrated in reference [33]. The acid concentration varies as the partial pressure of the water is reduced or increased. Combined with the actual partial pressure of water vapor, pressure is the driving force of the evaporation and hence of the volume change.

The influence of the doped acid and absorbed water on the volume swelling for acid-doped PBI membranes was studied and found the effect of swelling by water to be negligible [45]. Our model predicts the concentrations as shown in Fig. 10. At 90-mV cell voltage, the mole fraction, X_{H3PO4}, ranges from 0.77 to 0.74 for anode side and ranges from 0.81 to 0.79 for cathode side. Further at the outlet, the flow channels contain more water vapor because of the higher rate evaporation. The phosphoric acid distribution depends on, e.g., the water pressure and temperature and undergoes concentration changes when changing the load current. The concentration of H_3PO_4 decreases at the outlet of the gas channels, mainly due to the temperature variation in the membrane causing eventual evaporation rates of H_3PO_4 where the evaporation rate is increased with increasing temperature. It is also noted that the mole fractions on the cathode side are slightly higher; this is probably due to the fact that the cathodic compartment generally presents lower temperatures at the entrance of the flow channel, increasing slightly towards the outlet channel. Thus, because the anodic side has higher temperatures than that cathodic side, the rate of acid evaporation is increased as the temperature rises, causing the lower concentration of phosphoric acid on the anode side. The distribution of phosphoric acid in catalyst-membrane interface is similar when using hydrogen as fuel, as has also been demonstrated elsewhere [11].

Figure 11 shows the diffusive flux magnitude ($kgm^{-2}\ s^{-1}$) of O_2 at 90 mV. The diffusive flux of oxygen is directly related to the temperature distribution in the membrane, also implying the distribution of phosphoric acid, where the diffusive flux increases with increasing temperature (see Fig. 7)

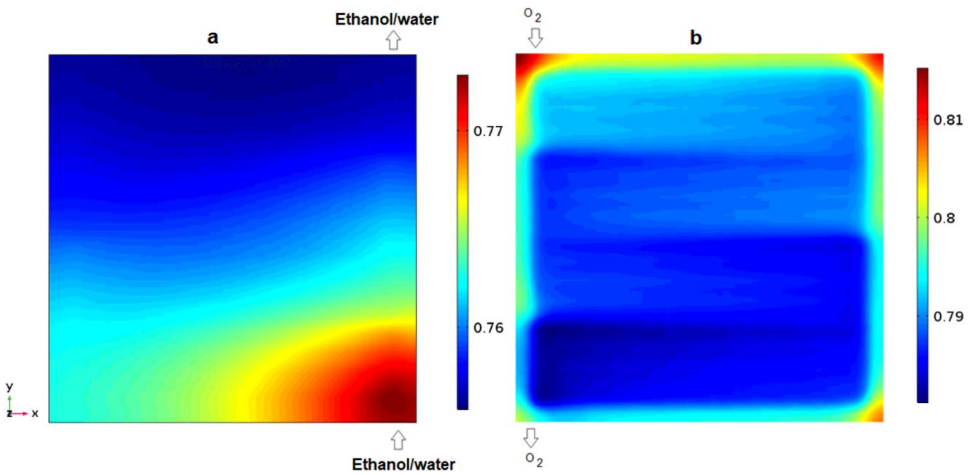

Fig. 10 Phosphoric acid mole fraction catalyst-membrane interface at 90 mV: **a** anode side, **b** cathode side

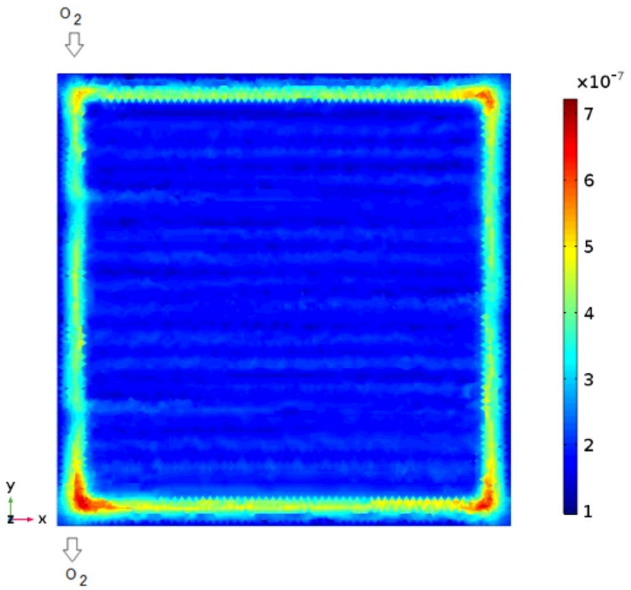

Fig. 11 Diffusive flux magnitude of O_2 at 90 mV

where the temperature at the oxygen inlet is lower. It is also observed that the diffusive flux of oxygen presents the same distribution as shown in Fig. 8 (mainly at the edges).

Figure 12 shows the mass fraction of ethanol and water at a potential of 90 mV in anode side. It is worth mentioning that the ethanol supply was carried out (inlet) through the lower part of the plate, while the exit (outlet) of excess ethanol (unreacted ethanol) and water was conducted in the upper part of the flow plate. As expected, the mass fraction of ethanol decreases along the flow channels towards the outlet channels. The ethanol concentration for this profile significantly decreased along with the anode catalyst layer due to the electrochemical reaction between ethanol and oxygen. While water concentration increases due to back diffusion of water vapor. Also, when ethanol cross and reacted at the anode catalyst layer, most of them had been used up. A small amount of unreacted ethanol crosses to the cathode side through the membrane, resulting in the ethanol crossover. The mass fraction of ethanol decreases mainly due to crossover as well as the interference of the back diffusion of water on the anode side.

Conclusion

The effects of temperature on heat, mass, and charge transports occurring in the PBI/H_3PO_4 membrane feed by ethanol were developed, modeled, and solved using computational fluid dynamics (CFD) software (COMSOL Multiphysics 3.5a). Polarization curves was simulated and compared to the experimental data. The model showed consistency and was used to investigate the behavior of H_3PO_4 concentration and all transport characteristics. However, the concentration of phosphoric acid decreases with increasing temperature and relative humidity. It was also noted that the concentration of phosphoric acid in ethanol depends mainly on the temperature distribution in membrane and the water vapor pressure, very similar result when hydrogen is used as fuel. Ethanol concentration has enormous impacts on fuel cell performance. The current distribution tends to be concentrated at the edges near the inlet and outlet of the gas, with the current decreasing as the O_2 reaches the center of the flow channels. Such a feature can be strictly associated with the ethanol crossover, which can lead to mixed potential and non-uniform current distribution. In contrast to current distribution, oxygen diffusive flow presents to be more homogeneous, indicating that if the current is mainly related to O_2 reduction, the current distribution should also be homogeneous, reinforcing the hypothesis of strong influence of ethanol resulting from crossover in the cathodic current distribution response. These findings can be considered the main contributions of this work.

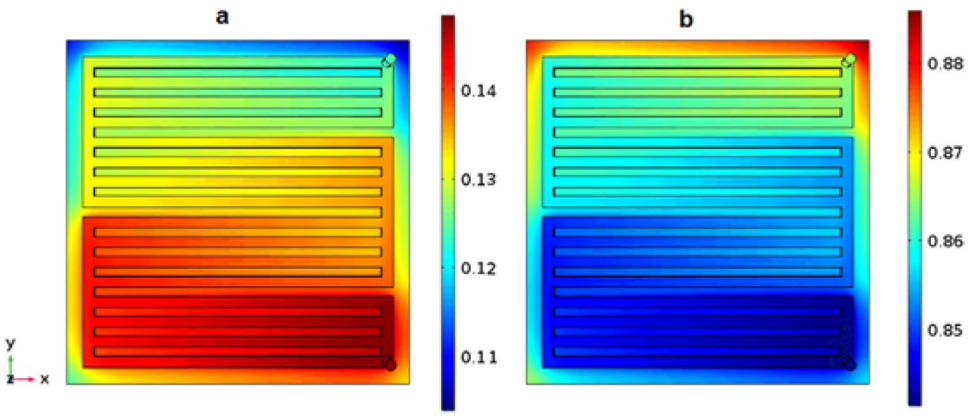

Fig. 12 Mass fraction at 90 mV **a** ethanol and **b** water

List of symbols

b: Tafel coefficient; c_p: Specific heat capacity/J kg^{-1} K^{-1}; D_i^T: Thermal diffusion coefficient/m^2 s^{-1}; $D_i^{\hat{k}}$: Effective diffusivity/m^2 s^{-1}; D_{ejk}: Binary diffusion coefficient/m^2 s^{-1}; DEFC: Direct ethanol fuel cell; E_{eq}: Equilibrium potential/V; F: Faraday constant/96487 C mol^{-1}; h: Convective heat transfer coefficient/W m^{-2} K; i: Electronic current/A m^{-2}; i_0: Exchange current density/A m^{-2}; i_{0ref}: Reference exchange current density/A m^{-2}; J_i: Diffusion flux/kg m^{-2} s^{-1}; k: Thermal conductivity/W m^{-1} K^{-1}; M: Molecular weight/kg mol^{-1}; $m_{H_{3PO_4}}$: Mass fraction of H_3PO_4; N_i: Total flux of species/kg m^{-2} s^{-1}; p: Pressure/Pa; R: Universal gas constant/8.3143 J mol^{-1} K^{-1}; S_m: Source term for conservation of momentum/kg m^{-3} s^{-1}; S_s: Source term for conservation of species/mol m^{-3} s^{-1}; S_e: Source term for conservation of energy/W m^{-3}; S_{sol}: Source term for conservation of charge/A m^{-3}; S_{men}: Source term for conservation of charge/A m^{-3}; T: Temperature/K; X_{H3PO4}: Mole fraction of H_3PO_4

Greek symbols

α: Transfer coefficient; ε: Porosity; ε_{PBI}: Volume fraction of electrolyte in CL; η: Overpotential/V; I: Identity tensor; k: Permeability of the porous media/m^2; $\boldsymbol{\lambda}$: Mean free path average/nm; μ: Dynamic viscosity/Pa s; T: Transpose; ρ: Density/kg m^{-3}; σ: Conductivity/S m^{-1}; ϕ: Electric potential/V; ω_i: Mass fraction of species

Superscripts and subscripts

a: Anode; BP: Bipolar plate; c: Cathode; CL: Catalyst layer; ext: External; GDL: Gas diffusion layer; H_3PO_4: Phosphoric acid; H_2O: Water; H_2: Hydrogen; l: Electrolyte; mem: Membrane; MEA: Membrane electrode assembly; O_2: Oxygen; PBI: Polybenzimidazole; STP: Standard conditions for temperature and pressure; sol: Solid phase excluding the membrane electrolyte; s: Electrode

Acknowledgements The authors are grateful for the support of the Center for Innovation on New Energies CINE-SHELL (ANP)/FAPESP (2017/11937-4), CNPq, CAPES, and CNEN. Thanks are also due to the funding supports FAPESP 2014/09087-4.

References

1. Authayanun S, Im-orb K, Arpornwichanop A (2015) Sciense Direct 473:36
2. Song S, Tsiakaras P (2006) Recent progress in direct ethanol proton exchange membrane fuel cells (DE-PEMFCs). Applied Catalysis B 63:187–193
3. Dresch MA, Matos BR, Godoi DRM, Linardi M, Fonseca FC, Villullas HM, Santiago EI (2021) Advancing direct ethanol fuel cell operation at intermediate temperature by combining Nafion-hybrid electrolyte and well-alloyed PtSn/c electrocatalyst. Int J Hydrogen Energy 46:13252
4. Ahmed Z, Matos BR, Florio DZ, Rey JFQ, Santiago EI, Fonseca FC (2016) Nafion-mesoporous silica composite electrolyte: properties and direct ethanol fuel cells performance. Mater Renew Sustain Energy 5:6
5. Walkowiak-Kulikowska J, Wolska J, Koroniak H (2017) Polymers application in proton exchange membranes for fuel cells (PEMFCs). Phys Sci Rev 20170018
6. Qingfeng Li Q, Jensena J, Savinell RF, Bjerrum NJ (2009) High temperature proton exchange membranes based on polybenzimidazoles for fuel cells. Prog Polym Sci 34:449–477
7. Javier P, Rao CV, Sundara L, Rambabu GB (2011) Electrochemical performance measurements of PBI-based high-temperature PEMFCs. Int J Electrochem 261065
8. Lobato J, Canizares P, Rodrigo MA, Linares JJ, Pinar FJ (2010) Study of the influence of the amount of PBI–H3PO4 in the catalytic layer of a high temperature PEMFC. Int J Hydrog Energy 35:1347–1355
9. Tang D, Wang X, Zhao W, Wang S, Zhu Z (2015) Modeling and simulation of mass transfer process of tubular cathode in direct ethanol fuel cell. Electrochem 83:962–968
10. Xu G, Tang D, Han Y (2022) Simulation of the effect of novel porous channels and their optimizations on the performance of direct ethanol fuel cell. J Energy Eng 148:04022020
11. Panesi ARQ, Silva RP, Cunha EF, Korkischko I, Santiago EI (2021) Three-dimensional CFD modeling of hydrogen HT-PEMFC based on H_3PO_4-doped PBI membranes. Ionics
12. Sokmez E, Taymaz I, Kahveci EE (2022) Performance evaluation of direct ethanol fuel cell using a three-dimensional CFD model. Fuel 313:123022
13. Silva RP (2019) Desenvolvimento de membranas não-fluoradas a base de PBI para aplicação em células a combustível de etanol direto de alta temperatura IPEN
14. Fuel Cell Store, Fuel Cell Modeling Basics, Material Information can be found under: https://www.fuelcellstore.com/blog-section/fuel-cell-modeling-basics. Accessed Sep 2022
15. Linares J, Thairo J, Rocha A, Sabrina Zignari A (2013) Valdecir Paganin, R. Ernesto Gonzales. Int J Hydrog Energy 630:38
16. Maia KK, de Souza Jr R (2017) J Appl Electrochem 47:37
17. ZOLTEK, Material Information can be found under. https://pdf.directindustry.com/pt/pdf-en/zoltek/panex-30-brochure/38933-575644.html#open. Accessed Sep 2022
18. Sohn Y-J, Kim M, Yang T-H, Kim K (2011) Int J Hydrogen Energy 15273:23
19. Huang H, Zhou Y, Hao Deng Xu, Du Xie Q, Yin Y, Jiao K (2016) Int J Hydrogen Energy 3113:41
20. Rasheed RKA (2016) Siew Hwa Chan. Electrochim Acta 280:222
21. Chippar P, Hyunchul Ju (2013) Int J Hydrogen Energy 7704:38
22. Chippar P, Hyunchul Ju (2012) Solid State Ionic 30:225
23. Xia L, Zhang C, Minghui Hu, Jiang S (2018) Cheng Siong Chin, Zuchang Gao, Quan Liao. Int J Hydrogen Energy 23441:43
24. Wang Y, Sauer DU, Koehne S, Ersoez A (2014) Int J Hydrogen Energy 19067:39
25. Ubong EU, Shi Z, Wang X (2009) J Electrochem Soc B1276:156
26 Kamal Raj, Zhang Caizhi, Quan Liao SH, Chan, (2017) Int J Hydrogen Energy 3142:42
27. Yin Y, Wang J, Yang X, Qing Du, Fang J, Jiao K (2014) Int J Hydrogen Energy 13671:39
28. Siegel C, Lang S (eds) (2016) Fontes. Springer International Publishing, Peter Beckhaus
29. MacDonald DI, Boyack JR (1969) Chem Eng Data 14:380–384
30. Siegel C (2015) High temperature polymer electrolyte membrane fuel cells: modeling, simulation, and segmented measurements
31. Elden G, Çelik M, Genç G, Yapıcı H (2016) Energy 772:103

32 Cheddie Denver F, Munroe Norman D. H (2007) Int J Hydrogen Energy 832:32
33. Hong S, Chen X, Hao C, Saif A (2015) Appl Energy 160:944
34. He R, Li Q, Bach A, Jensen JO, Bjerrum NJ (2006) J Membr Sci 38:277
35. Jiao K, Li X (2010) Fuel Cells 351:10
36. Liu H, Li P, Hartz A, Wang K (2015) Int J Energy Environ Eng 75:6
37. Ruy Souza Jr (2008) Daniela Marques dos Anjos, Germano Tremiliosi Filho, Ernesto Rafael Gonzales, Christophe Coutanceau, Eric Sibert, Jean- Michel Léger, Kouakou Boniface Kokoh. J Power Sources 293:180
38. Su A, Ferng YM, Hou J, Yu TL (2012) Int J Hydrogen Energy 7710:9
39. COMSOL MULTIPHYSICS. Batteries & fuel cells module user's guide materials library. Material Information can be found under: https://doc.comsol.com/5.4/doc/com.comsol.help.bfc/BatteriesAndFuelCellsModuleUsersGuide.pdf
40. Kreith F and Bohn MS (2003) Princípios de Transferência de calor. Thomson
41. Jiao K, Ibrahim Alaefour E, Li X (2011) Fuel 568:90
42. Sousa T, Mamlouk M, Scott K (2010) Fuel Cells 693:10
43. Li G, Pickup PG (2006) J Power Sources 263:161
44. Kazdal TJ, Lang S, Kühl F, Hampe MJ (2014) J Power Sources 446:249
45. Sousa T, Mamlouk M, Scott K, Rangel CM (2012) Fuel Cells 566:12